ROYAL SOCIETY
OF CHEMISTRY

PAPER

Check for updates

A biocompatible two-photon absorbing fluorescent mitochondrial probe for deep *in vivo* bioimaging†

Lingmin Lin, †abc Zewei He,†d Tianfang Zhang,†a Yanming Zuo,c Xiangfeng Chen,bc Zeinab Abdelrahman,bc Feihong Chen,d Zhongcao Wei,e Ke Si,d Wei Gong,f Xuhua Wang, *bcg Sailing He *d and Zuobing Chen*a

Mitochondria, key organelles which keep in tune with energy demands for eukaryotic cells, are firmly associated with neurological conditions and post-traumatic rehabilitation. *In vivo* fluorescence imaging of mitochondria, especially with deep tissue penetration, would open a window to investigate the actual context of the brain. However, the depth of traditional two-photon mitochondrial fluorescence imaging is still limited due to the poor biological compatibility or low two-photon absorption cross-sections. A biocompatible mitochondria-targeted two-photon fluorescent dye (**FO2**) with an excellent two-photon absorption cross-section (the maximum of 1184 GM at 790 nm) and low cellular toxicity was designed and synthesized to overcome this problem. With this dye, we reached an imaging depth of *ca.* 640 μm during mitochondrial imaging of cortical cells in live animals. **FO2** could be an excellent mitochondrial probe for live animal neural imaging to investigate the function and dysfunction of mitochondria in the brain.

a Department of Rehabilitation Medicine, First Affiliated Hospital, College of Medicine, Zhejiang University, Hangzhou, Zhejiang Province, 310003, China. E-mail: czb1971@zju.edu.cn

b Department of Neurobiology and Department of Orthopedics, 2nd Affiliated Hospital, Zhejiang University School of Medicine, Hangzhou, Zhejiang Province 310009, China. E-mail: xhw@zju.edu.cn

c NHC and CAMS Key Laboratory of Medical Neurobiology, MOE Frontier Science Center for Brain Research and Brain-Machine Integration, School of Brain Science and Brain Medicine, Zhejiang University, Hangzhou, Zhejiang Province, 310003, China

d State Key Laboratory for Modern Optical Instrumentation, Centre for Optical and Electromagnetic Research, East Building No. 5, Zijingang Campus. and Zhejiang University, Hangzhou 310058, China. E-mail: sailing@kth.se

e Guangdong Provincial Key Laboratory of Nanophotonic Functional Materials and Devices, School of Information and Optoelectronic Science and Engineering, South China Normal University, Guangzhou 510006, China

f Center for Neuroscience and Department of Neurobiology of the Second Affiliated Hospital, State Key Laboratory of Modern Optical Instrumentation, Zhejiang University School of Medicine, Hangzhou 310058, China

g Co-innovation Center of Neuroregeneration, Nantong University, Nantong, 226001 Jiangsu, P. R. China.

† These authors contributed equally

Electronic supplementary information (ESI) available: The following files are available free of charge. Fig. S1–S8 (PDF). Fig S1: Structure representation of FO2. Fig. S2: Structure representation of compound 2. Fig. S3: Structure representation of compound 6. Fig. S4: Structure representation of compound 7.Fig.S5:The respondent characters of FO2. Fig. S6: Colocalization analysis of FO2 and lysosomes. Fig. S7: The stack of FO2 in vivo imaging in mice cortex. Fig. S8: Two-photon colocalization in vivo. See DOI: 10.1039/d1tb02040d

1. Introduction

Mitochondria, double-membrane organelles crucial for energy production in eukaryotic cells, play fundamental roles in cellular metabolism and signal transduction.[1] Neuronal death and axon degeneration happened after the central nervous system (CNS) injury, in which a hypoxic-ischemic and inflammatory micro-environment exacerbates the lesion site to a worse outcome. It is well known that axonal regeneration, a prerequisite step for the rehabilitation process, is highly energy-demanding. Recent studies indicated that mitochondria play pivotal roles in promoting axonal regrowth and synaptic plasticity by supplying energy and fueling local translation after CNS injury such as ischemic stroke.[2–5] However, how mitochondria respond to neuronal damage in a live mouse model remains unknown mainly due to the lack of deep *in vivo* mitochondrial imaging technology. Therefore, an *in vivo* mitochondrial imaging technology with deep CNS tissue penetration is desperately desired to investigate the mechanism underpinning these axonal regrowth and synaptic plasticity processes during neurological rehabilitation.

Compared with traditional one-photon techniques, two-photon fluorescence imaging (TPFI) employs low-energy near-infrared (NIR) rays (700–1000 nm) to generate high-energy visible fluorescence. This merit leads to less tissue scattering and reduced photobleaching, contributing to excellent spatial

resolution in deep *in vivo* bioimaging.[6] One key factor related to the maximum achievable depth in two-photon imaging is the brightness, which incorporates both the two-photon absorbing ability and the fluorescence quantum yield of two-photon probes.[7] Because of the substantially negligible two-photon absorption (2PA) cross-sections of traditional mitochondrial trackers, it demands relatively high pulse energies to increase the imaging depth, which causes more photodamage to live tissues. Therefore, the spectroscopic characteristics of mitochondrial trackers need to be optimized to increase the penetration depth with minimum cytotoxicity.[8]

Recently, several fluorescent probes with relatively high two-photon absorbing capacity have been introduced to break through the depth limitation of mitochondrial imaging.[9–11] For example, a mitochondrial probe QBMP synthesized with a favorable 2PA cross-section (70.5 GM) achieved a tissue penetration depth of 225 μm in *in vivo* bioimaging.[9–11] However, these mitochondrial probes still suffer from low two-photon absorption properties[11–13] or poor biocompatibility,[14,15] restricting their application in live animal bioimaging. This study developed a water-soluble probe with low cytotoxicity and a relatively high 2PA cross-section of *ca.* 1184 GM for mitochondrial imaging with a tissue penetration depth of *ca.* 640 μm during brain mitochondrial imaging based on a novel strategy of chemical design. This mitochondrial probe (**FO2**) is promising to be a powerful biomedical tool to investigate the mitochondrial response to neuronal injury and uncover the mechanism underpinning the axonal regrowth and synaptic plasticity processes during neurological rehabilitation.

2. Results and discussion

2.1. Design, synthesis, and structure of FO2

Great interest in the development of novel organic nonlinear optical materials has driven many strategies for multi-photon probes, such as D–π–D,[16] D–π–A–π–D,[17] and D–π–A.[18] Herein, the core backbone of the synthesized probe, named **FO2**, was designed as a central fluorene-derived structure (9,9-bis(2-(2-methooxyethyl)-9*H*-fluorene residue)) with vinylic linkage to benzine and methylazane to form a fluorene-derived D–π–D backbone; the structure, as previously illustrated, tended to exhibit high two-photon absorption properties through large intramolecular charge transfer.[19–21] In addition, we also attached an acetate laterally in order to target mitochondria, the strategy transfer from previous research, where the carboxylate group enabled a passive diffusion into the cell membrane and targeted mitochondria (Scheme 1).[22] The bilateral carboxylate (polar heads) of the carbon skeleton would form a bola amphiphile, which yields a higher water solubility and a decreased aggregation than traditional single-head amphiphiles.[23] Besides, the oxyethylene groups included to the side chains would further enhance the water-solubility.[21] Hence, we would be able to obtain a water-soluble mitochondrial probe with high two-photon absorption properties.

Briefly, as shown in Scheme 1, 2,7-dibromo-9,9-bis(2-(2-methoxyethyl)ethyl)-9*H*-fluorene (compound **2**, Fig. S2, ESI†)

and methyl *N*-(4-bromophenyl)-*N*-methylglycinate (compound **6**, Fig. S3, ESI†) were separately synthesized and mixed proportionally following a 12-hour reaction of the mixtures in dioxane solution using a Pd(dppf)Cl$_2$/Cs$_2$CO$_3$ catalytic system (to produce compound **7**, Fig. S4, ESI†). The final product of the reaction was then alkalized and purified, producing the resultant **FO2** (Fig. S1, ESI†) in a 39.65% yield. The synthesis process and the key products in the route are represented in Fig. S1–S4 (ESI†).
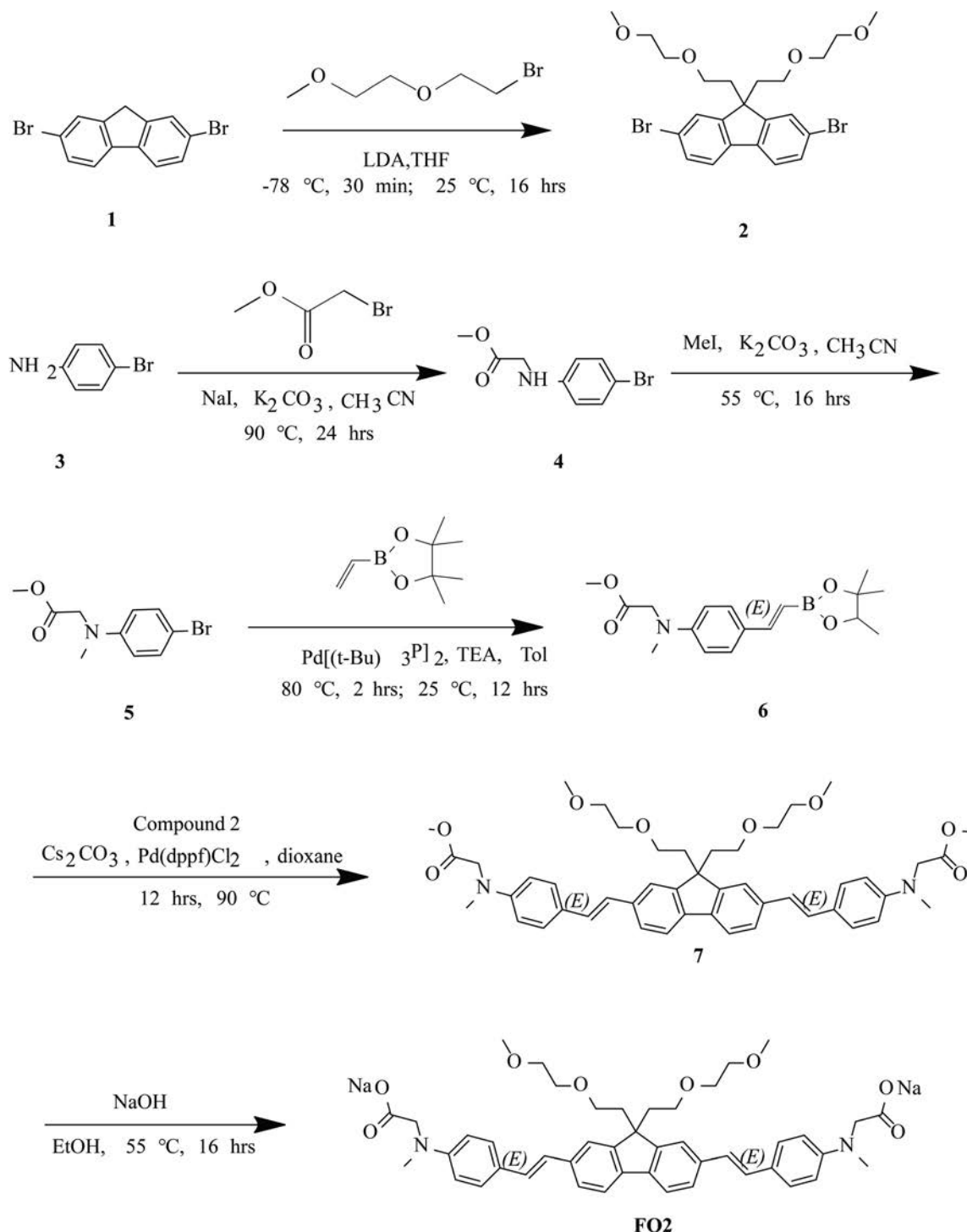
The structure of **FO2**, sodium 2,2′-(((((1*E*,1′*E*)-(9,9-bis(2-(2-methoxyethyl)ethyl)-9*H*-fluorene-2,7-diyl)bis(ethene-2,1-diyl))-bis(4,1-phenylene))bis(methylazanediyl))diacetate, is presented in Scheme 1. The mass spectrum calculated for C$_{45}$H$_{52}$N$_2$O$_8$ was 748.3735 and found 748.3722 (Fig. S1a, ESI†). The proton NMR data of **FO2** are: HNMR of Target 1 (400 MHz, DMSO-d$_6$): δ = 7.74 (br s, 2H), 7.67 (br d, J = 7.8 Hz, 2H), 7.45 (br d, J = 7.5 Hz, 2H), 7.37 (br d, J = 8.3 Hz, 4H), 7.20 (br d, J = 16.1 Hz, 2H), 6.99 (br d, J = 16.1 Hz, 2H), 6.60 (br d, J = 8.5 Hz, 4H), 3.64 (br s, 4H), 3.18 (br d, J = 4.8 Hz, 4H), 3.10 (s, 10H), 3.00 (s, 6H), 2.67 (br s, 4H), 2.38 (br s, 4H), as shown in Fig. S2b (ESI†). And the carbon-13 NMR showed δ 177.48, 169.06, 149.57, 149.49, 139.12, 137.69, 128.54, 127.16, 125.41, 125.28, 123.50, 119.99, 119.52, 111.75, 71.28, 69.22, 66.95, 57.63, 56.65, 50.87, 39.16, 38.50, 22.85 (Fig. S1c, ESI†). These representations of **FO2** supported the theoretical structure of **FO2** illustrated in Fig S1 (ESI†).

2.2. Photophysical properties of FO2

Since the linear and nonlinear photophysical properties are important for nonlinear bioimaging applications, the optical characteristics of this probe were investigated. The targeted product **FO2** was brown in solid powder and yellow in diluted solution (Fig. 1a). The maximum absorption of **FO2** was λ_{ab} = 403 nm in deionized water and PBS (phosphate buffer saline, pH = 7.4), with the molar absorption coefficient of **FO2** in deionized water (λ_{ab} = 405 nm) being 4.05 × 10^4 M^{-1} cm^{-1} (Fig. 1b). The one-photon emission spectra showed a maximum emission at 540 nm excited by a laser at 405 nm in aqueous solutions (Fig. 1a), which is similar to many probes for *in vivo* two-photon imaging, such as GFP, GCaMP6 and OGB-1.[24–27]

In the following test, we found that **FO2** was sensitive to solvent polarity (Fig. S5a and b, ESI†), and the emission spectra exhibited larger bathochromic shifts in aqueous solution (Fig. S5b and c, ESI†). However, the polarity in DMSO-water binary mixture with various volume ratios (DMSO, D8371, purity > 99.5%; Solarbio, Beijing, China) did not significantly shift the emission bands compared to other solvents (Fig. S5c, ESI†). Such a trend might be due to the simultaneous presence of hydrophobic and hydrophilic groups in DMSO with specific hydrogen connection with H$_2$O.[28,29]

The optical properties of **FO2** in different pH environments were also investigated to assay its response to pH variations.[30,31] To this end, the absorbance and emission of **FO2** in a series of phosphate buffers with different pH values from 4.9 to 12.0 were measured. We found that the optical density of **FO2** in the buffers with the same concentration was doubled at 405 nm in an alkaline environment among the tested range with an iso-absorptive point at pH = 7.5. This phenomenon occurred possibly

Scheme 1 Synthesis route of **FO2**. **FO2**, sodium 2,2′-((((1E,1′E)-(9,9-bis(2-(2-methoxy ethoxy)ethyl)-9H-fluorene-2,7-diyl)bis(ethene-2,1-diyl))bis(4,1-phenylene))bis(methyl azanediyl))diacetate, was synthesized using two key chemicals, compound **2** (2,7-dibromo-9,9-bis(2-(2-methoxy ethoxy)ethyl)-9H-fluorene) and compound **6** (methyl N-(4-bromo phenyl)-N-methyl glycinate), by an alkalization process.

because of less aggregation of **FO2** in alkaline environments. And the pH environments did not shift the maximum absorption and emission spectra of **FO2** significantly (Fig. S5d and e, ESI†).

Besides, the viscosity sensitivity was studied using the glycerol–methanol system (Fig. S5f and g, ESI†).[32,33] In a highly

viscous environment, the fluorescence intensity was drastically decreased. The primary mechanism ascribed to the quenching phenomenon should be the π–π stacking upon aggregate formation due to the restricted intramolecular motion (aggregation-caused quenching, ACQ) in high viscosity, which
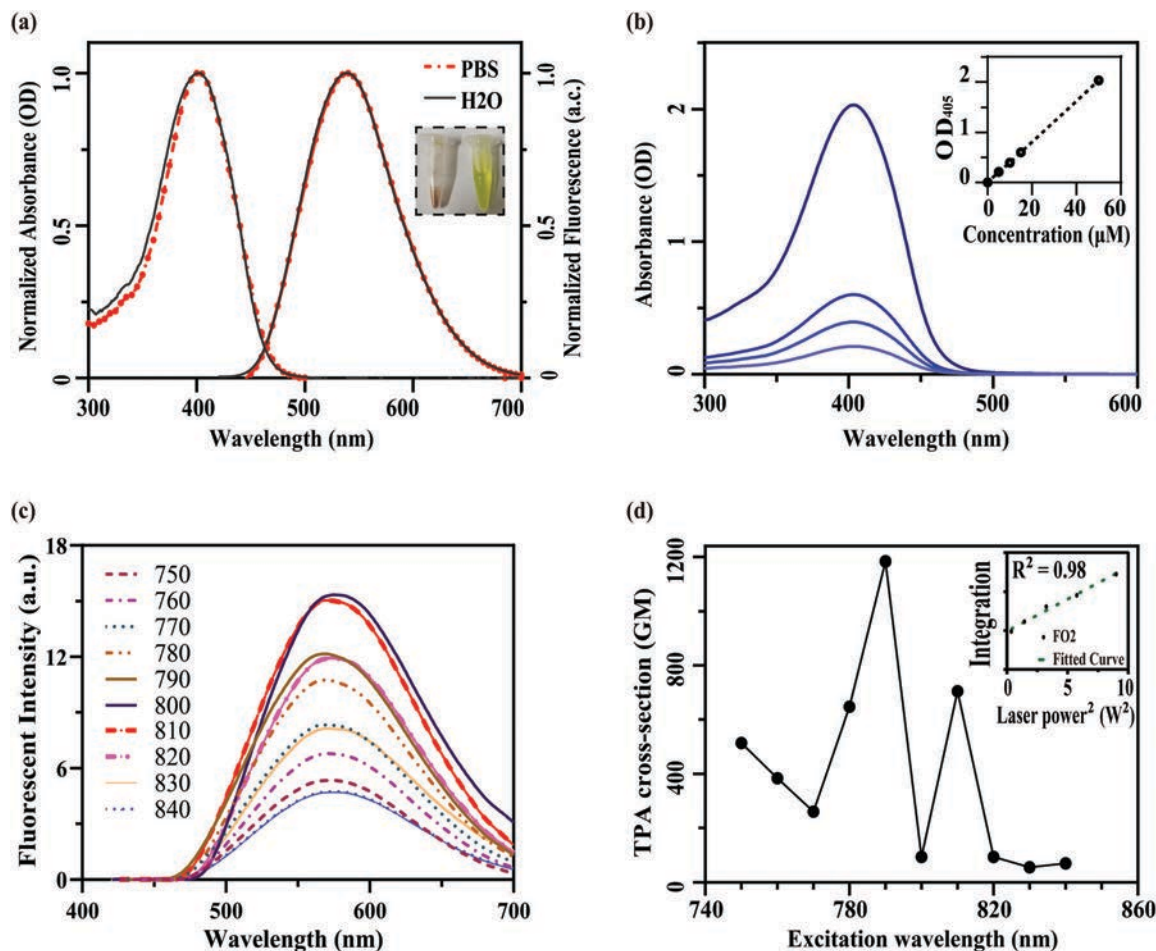
Fig. 1 Optical properties of **FO2**. (a) Normalized absorbance and one-photon fluorescence spectra (λ_{Ex} = 405 nm) of **FO2** in different solutions (10 uM deionized water, H_2O, black line; phosphate buffer saline with a pH of 7.4, PBS, red dotted dash line; and DMSO, dimethyl sulfoxide, blue dash line). Various conditions of **FO2** were also presented, brown in solid powder and yellow in dilute solution. (b) The molar absorption of **FO2** was 4.05 $\times$ 10^4 M^{-1} cm^{-1} at 405 nm in deionized water with a goodness of fit R^2 of 0.9996, calculated through the absorption spectra of gradient concentrations. (c) Two-photon emission spectra induced the Ti: sapphire femtosecond lasers (from 750 nm to 840 nm, per 10 nm) in deionized water were calibrated to be the same concentration (2 mM); (d) the Two-photon absorbance (TPA) cross-sections of **FO2** were presented in GM (1 GM = 10^{-50} cm^4 s photon^{-1} molecule^{-1}), in which a nonlinear optical transition in two-photon detection was confirmed with the linearity of the emission intensity of **FO2** and the squared laser power typically at 800 nm (R^2 = 0.978).

is very common especially for those luminophores with planar structures (like **FO2**).[34]

Meanwhile, the response of a series of bio-analytes (such as potential nucleophiles, SO_2 and H_2S) and other biologically relevant species (H_2O_2 and NaClO) was tested. We applied Na_2S as an H_2S donor, Na_2SO_3 and $NaHSO_3$ (with different pH values) as SO_2 donors, plus reduced glutathione (GSH) to test the correspondence of **FO2** for reactive sulfur species (the same incubating time as in the previous study).[35] However, we did not find a robust selectivity among these chemicals (*e.g.* $NaHSO_3$ and Na_2SO_3). Instead, the slightly acidic GSH, $NaHSO_3$, and H_2O_2, and alkaline NaClO, Na_2SO_3, and Na_2S seemed to exhibit a pH relevant absorbance (Fig. S5h and d, ESI†) and emission spectra (Fig. S5i and e, ESI†).

The fluorescence quantum yield of **FO2** was 89.0% in DMSO and 2.1% in aqueous solution, suggesting an aggregation quenching effect of this amphiphile probe in the polar water

solution. The self-assembly of **FO2** in water might bury the hydrophobic moieties in the nano-aggregates with more π–π stacking leading to non-radiative relaxation (aggregation-caused quenching, ACQ), a very common phenomenon in the field of luminophores.[23,34] The two-photon fluorescence spectra excited by femtosecond lasers with a series of wavelengths are shown in Fig. 1c. A linear regression of the two-photon fluorescence intensity integration and the square of the laser power confirmed a two-photon process with an R^2 of 0.978 (Fig. 1d). Using Rh6G as the standard, the maximum 2PA cross-section (δ) of **FO2** in deionized water was calculated to be 1184 GM excited by femtosecond lasers at 790 nm (Fig. 1d and Table 1), confirming our design with a high two-photon absorption value by a fluorene derived D–π–D skeleton.[16,19,20] Such a large δ value was higher than those of many reported mitochondria-targeting two-photon probes,[11,13,36] which is beneficial for two-photon deep tissue live animal imaging.

Table 1 Photophysical properties of **FO2**

	$\lambda_{Ab}{}^{a}$	$\lambda_{Em}{}^{b}$	Φ^{c}	$K_{b}{}^{d}$	$\delta\Phi^{e}$	$F_{M}{}^{f}$
FO2	404	530	2.1	0.2868	24.86	86.68
MTG	489^{g}	513^{g}	2.0^{g}	0.1090^{g}	2.18^{h}	20.00

^{a} λ_{Ab} refers to the wavelength at the peak of one-photon absorption spectra in nm. ^{b} λ_{Em} refers to the wavelength at the peak of one-photon fluorescence emission spectra in nm. ^{c} Φ, the fluorescence quantum yield (%). ^{d} K_{b}, photobleaching rate (per hour) measured by the speed of normalized decrease of fluorescence signals. ^{e} $\delta\Phi$, two-photon action absorption cross-section in GM $(10^{-50}\ cm^{4}\ s\ photon^{-1}\ molecule^{-1})$ calculated by the product of fluorescence quantum yield and two-photon cross-section. ^{f} FM, the figure of merit in GM·h. ^{g} Detected in deionized water (DMSO < 0.1%). ^{h} Reported in the literature.[38]

2.3. Higher figure of merit compared with a commercial mitochondrial probe

To compare the capacity of **FO2** with those of other probes for two-photon fluorescence microscopy, a defined figure of merit (FM) was adopted according to a reported method.[37] The FM comprehensively assessed the luminous efficiency and photostability by taking into account the fluorescence quantum yield (Φ), the 2PA cross-section (δ), and the photodecomposition quantum yield (η). The photostability of **FO2** and the commercially available mitochondrial tracker, MitoTracker Green (MTG), was investigated *via* a photodecomposition method described previously.[37] Even though the photodecomposition quantum yield (η) of **FO2** was lower than that of MTG, the two-photon action absorption cross-section[38] (equivalent to the product of Φ and δ) of **FO2** was one order of magnitude higher than the MTG's value. As a result, the FM of **FO2** was about four times higher than that of MTG (Table 1), suggesting that **FO2** is superior to commercial mitochondrial probes for TPFI.

2.4. Excellent specificity for mitochondria in cellular imaging

We next sought to investigate the specificity of **FO2** in mitochondrial imaging. Before that, the biocompatibility of **FO2** was assessed, and the results are illustrated in Fig. 2g. While the commercial mitochondrial probe (MitoTracker™ Deep Red FM, MTDR) showed a half inhibitory concentration of less than 1 μM, **FO2** did not significantly threaten cell survival up to a concentration of 20 μM, suggesting its low cellular toxicity (Fig. 2g). After verifying the biocompatibility, the mitochondria-targeting specificity of **FO2** was investigated by colocalization assays. In these experiments, C6 cells were co-incubated with **FO2** (λ_{ex} = 405 nm, λ_{em} = 430/530 nm) and MTDR (λ_{ex} = 635 nm, λ_{em} = 655/755 nm) or LysoTracker™ Deep Red (LTDR, λ_{ex} = 635 nm, and λ_{em} = 655/755 nm).[39] Typically, as shown in Fig. 2a–f, the fluorescence images of MTDR largely overlapped with that of **FO2** and exhibited an excellent colocalization in mitochondria with a high Pearson's correlation coefficient (0.90) and a Manders overlap coefficient (0.95). However, **FO2** and lysosomal probe LTDR were poorly colocalized with a low Pearson's coefficient of R = 0.386 (Fig S6, ESI†). The distinct colocalization coefficients (Fig. 2a–f and Fig. S6, ESI†) indicate that **FO2** tended to attach to mitochondria specifically.

2.5. Deep two-photon imaging with FO2 in live animals

To assess the TPFI capacity of **FO2** in live animals, we evaluated the maximum imaging depth by conducting TPFI through brain vessels. A cranial opening was performed, and the **FO2** was injected into the retro-orbital sinus of the operation mouse (Fig. 3a). And the TPFI images of the injected mouse reached a depth of about *ca.*1000 μm in our study (Fig. 3b and c). These results showed the superior ability of **FO2** in visualizing brain blood vessels, which is of vital importance for better understanding of the CNS injury, such as cerebral vascular occlusion, cerebral hemorrhage, and leukocyte extravasation.[8,40]

We next performed mitochondria-targeting TPFI of **FO2** in cortical cells in live animals. After the mice brain cortices were stereotaxically injected with a solution of **FO2** in saline, the mice were re-anesthetized and visualized under a two-photon microscope with excitation at 810 nm (Fig. 3d). We recorded the two-photon images of cortical cells up to a depth of *ca.* 640 μm from the fluorescent visualizable top (Fig. 3e–j and Fig. S7, ESI†), superior to other photosensors in live animal brain imaging.[41–43] In addition, the mitochondria, dot-shaped granules, could be clearly viewed in these cortical cells (white dashed box in Fig. 3i and Fig. S7, ESI†). More importantly, the two-photon colocalization *in vivo* imaging study also showed a high Pearson coefficient of R = 0.946 for **FO2** and MitoTracker Red, which suggested high mitochondrial specificity of **FO2** in live animals (Fig. S8, ESI†).

We assumed that the mitochondria-targetable properties of **FO2** might be attributed to its conjugation to the mitochondrial translocator protein.[22] Fluorescent dyes could electrostatically attract to mitochondria through their cationic structure or combine with mitochondria through specific structures, for example, the TOM complex in the outer membrane,[44] mitochondrial porin isoforms,[45] translocator protein,[46,47] and Mic60 of the inner membrane of mitochondria.[48] **FO2** was negatively charged with carboxylate tails, so it is unlikely that it gets electrostatically attracted to mitochondria. Similar to the mitochondrial probes with carboxylate (M-series),[22] **FO2** might target mitochondria through its conjugation to the translocator protein (TSPO), a five-transmembrane protein mainly located in the mitochondrial outer membrane.[46,47] This strategy was also employed by other mitochondria targeting fluorescence imaging studies. For example, a carboxylic end group was introduced onto the surface of TSPO-QD@SiO$_2$, rendering the quantum dot an ability to target mitochondria through conjugating to TSPO.[49]

The imaging depth of **FO2** might be further improved by shifting its absorption and emission spectra to the NIR regions. High-resolution deep imaging is unachievable for traditional linear fluorescence imaging or TPFI with low 2PA cross-sections in live animals because intact tissues strongly scatter light,[7] whereas TPFI employing **FO2** in this study pushed this limitation from *ca.* 250 μm to *ca.* 640 μm (Fig. S7, ESI†). Considering the fact that longer wavelengths would benefit less light scattering and deep tissue penetration,[7] the achievable imaging depth could be further improved by modifying **FO2**'s structure and shifting its absorption and emission spectra to the NIR
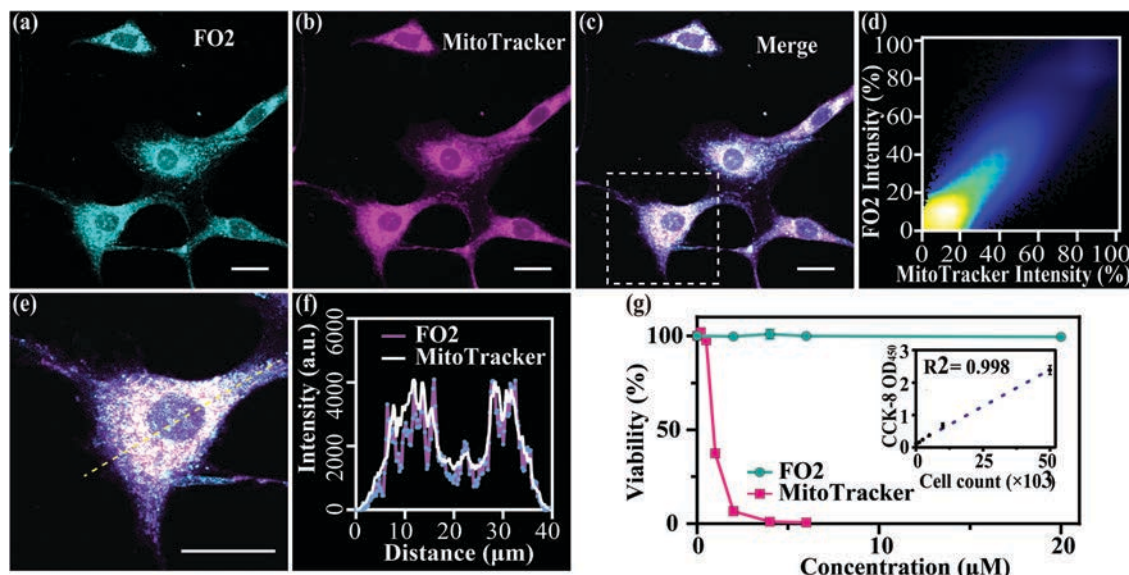
Fig. 2 *In vitro* one-photon imaging and the cytotoxicity of **FO2** in C6 cells. (a–d) Subcellular colocalization of (a) **FO2** (800 nM, 30 min; λ_{Ex} = 405 nm and λ_{Em} = 430/530 nm) and (b) Mitotracker Deep Red (100 nM, λ_{Ex} = 635 nm, λ_{Em} = 655/755 nm) in C6 cells were presented; (c) the overlapped images and (d) its scatter plot suggested a high specificity of **FO2** toward mitochondria (Pearson's coefficient 0.90 and Mander's overlap coefficient 0.95). Scale bar = 20 μm. (e) The enlarged picture of the box in subgraph (c) and (f) the linear signal distribution along its dashed line also depicted the colocalization properties of **FO2** and mitochondria. (g) Cell viability was measured following the commercial protocol of the CCK-8 kit, where **FO2** or Mitotracker Deep Red of different concentrations was incubated with C6 cells for 24 hours and CCK-8 agent for four hours. The reference fitting line of the cell numbers and the recorded optical density at 450 nm were depicted in the right up panel (R^2 = 0.998).

region *via* an extension of **FO2**'s π-system,[50] or fusing its parental fluorene with boron dipyrromethenes (BODIPYs).[51]

The aggregation-caused quenching, an extremely common phenomenon in the world of luminophores, is an unignorable issue of **FO2**, as uncovered in a highly viscous environment (Fig. S5f and g, ESI†).[34] In order to emit light efficiently when dispersed in aqueous solutions, we designed **FO2** with planar structures. However, as generally recognized, luminophores with a planar structure with aromatic groups easily suffer from intense π–π stacking leading to ACQ effects.[34,52] Although the phenomenon is very common in traditional probes, many strategies could be applied to decrease or even eliminate the ACQ in future modifications, such as incorporating aggregation-induced groups and changing the planar structures.[34]

3. Experimental

3.1. Materials and animals

Materials in the synthesis process, including (1) 2,7-dibromo-9*H* fluorene, (2) 1-(2-bromoethoxy)-2-methoxy-ethane, (3) 4-bromo-aniline, (4) methyl 2-bromoacetate, (5) CH₃CN, and (6) NaOH were purchased from Sigma-Aldrich.

Animals (female C57BL/C mice, 18 g, eight weeks) were obtained from the Laboratory Animal Center of Zhejiang University (Hangzhou, China) and kept in a dry and clean environment with enough food and water. All animal procedures were performed in compliance with the policy of animal ethics and approved by the ethic committee of Zhejiang University (ZJU20210172).

3.2. Synthesis

The synthesized pathway is presented in Scheme 1. The main products of each reaction were purified, and their mass spectra and magnetic resonance hydrogen spectroscopic data were examined accordingly. Generally, **FO2** was synthesized using 2,7-dibromo-9,9-bis(2-(2-methoxyethoxy)ethyl)-9*H*-fluorene (compound **2**) and methyl *N*-(4-bromophenyl)-*N*-methylglycinate (compound **6**) by an alkalization process (Scheme 1).

Specifically, compound **2** was produced by 2,7-dibromo-9*H*-fluorene and 1-(2-bromoethoxy)-2-methoxy-ethane (Scheme 1). 2,7-Dibromo-9*H* fluorene (20 g, 61.73 mmol) in tetrahydrofuran (300 mL) was added to lithium diisopropylamide (2 M, 77.16 mL) at −78 °C for 30 min, and then 1-(2-bromoethoxy)-2-methoxy-ethane (24.86 g, 135.80 mmol) was added at −78 °C. The mixture was stirred at 25 °C for 16 hours, quenched by 150 mL NH₄Cl (aq) at 0 °C, and then extracted with ethyl vinyl acetate. The combined organic layers were washed with 200 mL of brine, dried over Na₂SO₄, filtered, and concentrated under reduced pressure to give a residue. The residue was purified by flash silica gel chromatography (ISCO®; 80 g SepaFlash® silica flash column, eluent of 0–30% ethyl acetate/petroleum ether gradient @ 40 mL min⁻¹).

The synthesis of methyl *N*-(4-bromophenyl)-*N*-methylglycinate (compound **6**) was carried out using 4-bromoaniline and methyl 2-bromoacetate followed by the addition of methyl (Scheme 1). First, 4-bromoaniline (10 g, 58.13 mmol) and methyl 2-bromo-acetate (9.78 g, 63.95 mmol) dissolved in CH₃CN (150 mL) was added to NaI (3.49 g, 23.25 mmol) and K₂CO₃ (20.09 g, 145.33 mmol). The mixture was stirred at 90 °C for 24 hours and filtered through Celite. Then, the filtrate was concentrated under reduced pressure.
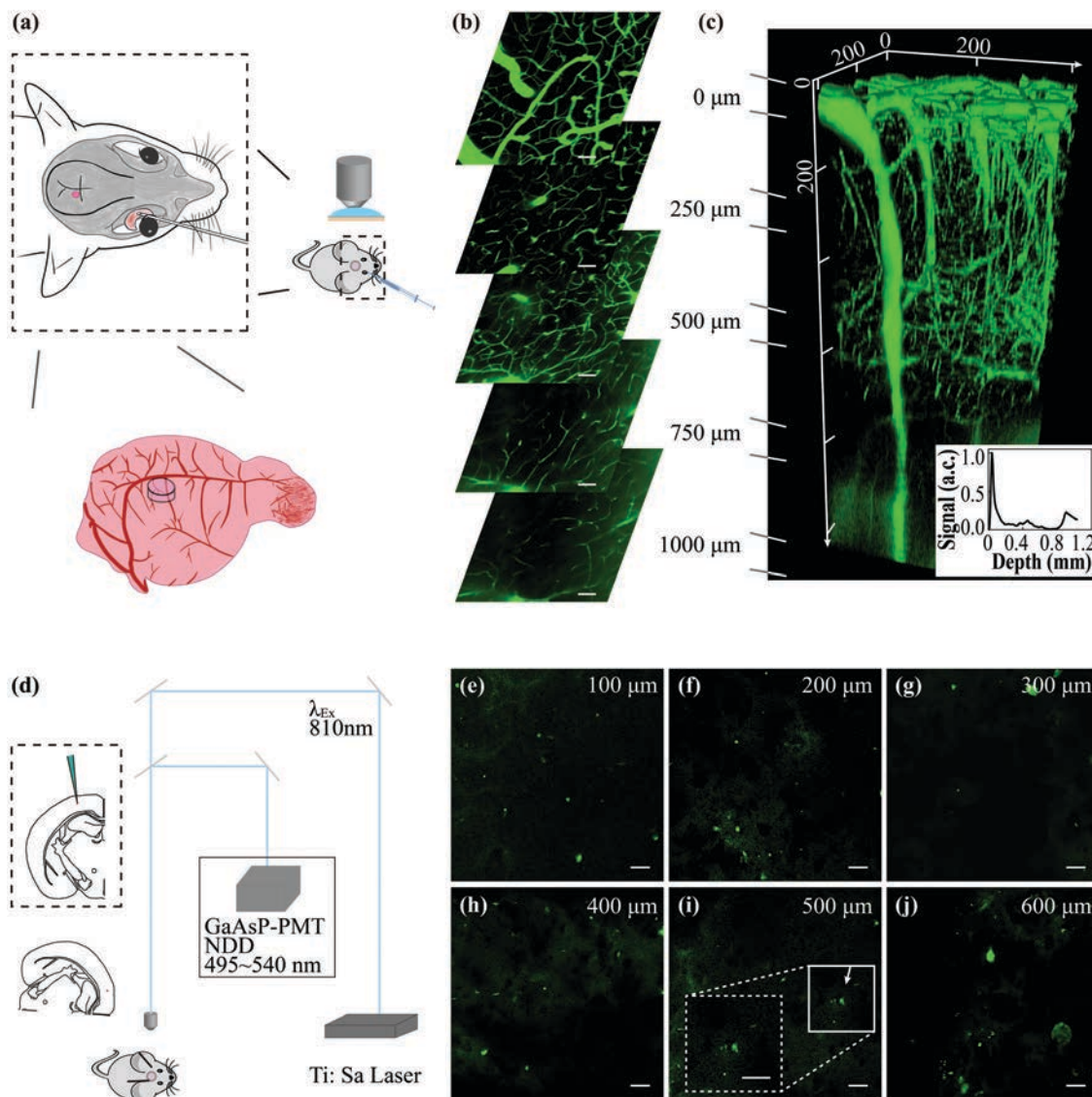
Fig. 3 *In vivo* imaging of **FO2** in mice cortex. (a) Illustration of retro-orbital venous sinus injection of **FO2** (100 μL, one millimolar per liter in normal saline) and *in vivo* vessel imaging. A circular craniotomy opening (1.5–2.0 mm diameter) was performed, and a customized metal plate was affixed to the open window following two-photon imaging with Ti: Sa Lasers (λ_{Ex} = 810 nm). (b) Cortex vessel images in the living mouse are illustrated with a thickness of 100 μm (scale bar = 50 μm) of depth up to 1035 μm (with the bottom-right inset showing the cross-sectional intensity profile) and (c) the three-dimensional reconstructed plot. (d) A diagram of stereotactic injection (1.5 mm lateral and 1.5 mm posterior to bregma) of **FO2** (80 nL per site, 0.2 mM in disinfected normal saline) in various depths (200 μm, 400 μm, and 600 μm) with the same craniotomy window as shown in (a) was depicted. Then the two-photon fluorescence images were recorded (495–540 nm) with non-linear excitation at 810 nm by the Ti: Sa Laser. (e–j) The two-photon imaging of the **FO2** probe after stereotactic injection (30 minutes). Scale bar = 20 μm. (i) The arrow indicate the enlarged cells in the white rectangular dashed box, showing dotted features of mitochondria *in vivo*.

The product, methyl (4-bromophenyl) glycinate (11 g, 45.07 mmol), was then mixed with MeI (7.56 g, 53.26 mmol) and K_2CO_3 (12.46 g, 90.13 mmol) in CH_3CN (50 mL) to obtain a methyl. The mixture was stirred at 85 °C for 16 hours. The reaction mixture was filtered through Celite, and the filtrate was dried under reduced pressure. The residue of the two reactions above was purified by flash silica gel chromatography (ISCO®; 40 g SepaFlash® silica flash column, eluent of 0–30% ethyl acetate/petroleum ether gradient @ 35 mL min^{-1} and 40 mL min^{-1} separately).

The final step is described below. Methyl *N*-(4-bromo-phenyl)-*N*-methylglycinate (5.8 g, 22.47 mmol) was first reacted with 4,4,5,5-tetramethyl-2-vinyl-1,3,2-dioxaborolane (5.19 g, 33.71 mmol) in toluene (100 mL) with triethylamine (4.55 g, 44.94 mmol) and palladium tritert-butyl phosphane (574.19 mg, 1.12 mmol), so that it could be appended to both sides of 2,7-dibromo-9,9-bis(2-(2-methoxyethoxy)ethyl)-9*H*-fluorene. After N_2 purging, two-hour heating (80 °C), and room temperature stirring (12 hours), the reaction mixture was filtered through Celite, collected under reduced pressure, and purified by flash silica gel chromatography (35 mL min^{-1}). And the product (5.2 g, 9.84 mmol) and 2,7-dibromo-9,9-bis(2-(2-methoxyethoxy)ethyl)-9*H*-fluorene (7.17 g, 21.66 mmol) in dioxane (100 mL) was added

to Pd(dppf)Cl$_2$ (720.25 mg, 984.34 umol) and Cs$_2$CO$_3$ (12.83 g, 39.37 mmol). The mixture was stirred at 90 °C for 12 hours. Then, the product, following filtration, concentration, and chromatography purification (ISCO®; 40 g SepaFlash® silica flash column, eluent of 0–70% ethyl acetate/petroleum ether gradient @ 40 mL min^{-1}), was obtained. Finally, it was alkalized by NaOH and reacted at 50 °C for 16 hours. The final product **FO2** was concentrated under reduced pressure and precipitated by centrifugation. We then examined its structure by liquid chromatography–mass spectrometry, proton nuclear magnetic resonance (NMR) spectroscopy, and carbon-13 NMR spectroscopy.

3.3. One-photon spectra of FO2 and selective studies

The one-photon absorption and emission spectra were recorded respectively using a UV-2500 series and an F-2500 FL spectrophotometer or a Thermo Varioskan Flash (Thermo Fisher Scientific, USA). The one-photon spectra of **FO2** were recorded in different solutions, including DMSO, PBS, and deionized water. An electronic microbalance was used to prepare the stack solutions of **FO2**. Final solutions of two milliliters titrated volume in 1.0 mL quartz cuvettes or 96-wells were tested.

As for the polarity, the $E_T(30)$ parameter was employed,[53,54] and the linearity of polarity and emission bands was calculated. The polarity of **FO2** in the DMSO/H$_2$O system with different volume ratios was calculated and the relative sensitivity was also tested.[55] The pH in phosphate buffer was confirmed by using a pH meter. The viscosity was tested by using the glycerol/methanol system, due to their well-distributed values.[32,33] The viscosity sensitive analysis was calculated by the linear regression coefficient of log Viscosity and log fluorescence at 500 nm (the Förster-Hoffmann function).[32] The selectivity of various bio-analytes was also tested by solvents of different bio-analytes, including nucleophiles potentially respondent towards **FO2** (NaHSO$_3$, Na$_2$SO$_3$ and NaS$_2$).[35]

3.4. Photostability

Working solutions of **FO2** (deionized water, 20 μM; λ_{ex} = 405 nm) and MTG (deionized water, DMSO < 0.1%; 10 μM; λ_{ex} = 488 nm) were prepared. According to the published protocol, fluorescence signals were recorded at 520 nm and 515 nm separately within two hours.[56,57] The photobleaching rate was calculated through the decrease percentage of normalized fluorescence signals with time.[58]

3.5. Fluorescence quantum yield determination

We determined the fluorescence quantum yields (Φ) of **FO2** in different solutions (deionized water and DMSO) based on the reference of Coumarin 153 (Φ = 0.53, EtOH) according to Levitus's tutorial.[59] First, we made a gradient dilution to obtain solutions of approximately 0.04 OD at the flat crest of the absorption spectra. Then we recorded their emission spectra using excitation wavelength, which is the same as the observed absorption wavelength.[59] Finally, the fluorescence quantum yields were calculated using the comparative method.[59]

3.6. Measurement of two-photon optical properties

A customized simple optical path was used to record the two-photon fluorescence spectra. A Ti:sapphire laser (Mira-HP, CA, USA) using pulsed femtosecond photons with indicated NIR wavelength (pulse width: 200 fs, repetition frequency: 76 MHz, laser power: 3 W) was employed to excite photosensors from the ground state (the Scheme). Two-photon fluorescence signals were received by an objective lens (20×, NA = 0.45) perpendicular to the direction of the signal light. To minimize the re-absorption effect, the excitation beam was focused as close to the side wall of the quartz cell as possible. We adopted lateral reception to reduce the influence of the femtosecond laser since the probability of scattered light diverges in all directions. Finally, the light signal passed an optical fiber with a 700 nm filter and was recorded using a high-speed PG2000 spectrometer (Ideaoptics, China). TPA cross-sections (σ) of **FO2** (deionized water) from 750 nm to 840 nm (per 10 nm) were calculated with a reference of Rh6G (MeOH, Φ = 0.93).[60] The TPA cross-section was calculated according to eqn (1).[61,62] The σ, F, N, and C represent the TPA cross-section, integration of fluorescence protons, reflection index of solvent, and solution concentration. The marks 1 and 0 represent **FO2** and the reference substance Rh6G.

$$\sigma_1 = \frac{F_1 \times \Phi_0 \times N_0 \times C_0}{F_0 \times \Phi_1 \times N_1 \times C_1} \times \sigma_0 \qquad (1)$$

3.7. Figure of merit (FM)

To compare the capacity of **FO2** with those of other probes for two-photon fluorescence microscopy, a defined figure of merit (FM), calculated as the product of their fluorescence quantum yield (Φ) and 2PA cross-section (δ) normalized by their photodecomposition quantum yield (η), i.e., FM = $\Phi\delta/\eta$, was employed according to the previous study.[37]

3.8. Cell culture and cell viability

The rodent glioma cells C6 were incubated in the Dulbecco's Modified Eagle Medium (DMEM, Corning, NY, USA), with the supplementation of 10% fetal bovine serum (HN-FBS-50; HAKATA, China) and 1% antibiotics (penicillin/streptomycin 10 000 U mL^{-1}, H8611; HAKATA, China). We seeded 5 × 10^3 cells in each well of 96-well microtiter plates and tested the cell viability with commercial Cell Counting Kit-8 (CCK-8, C0038; Beyotime, Shanghai, China). In detail, the cells were incubated in complete DMEM media for 24 hours in a humidified atmosphere with 5% CO$_2$ at 37 °C. **FO2** with gradient concentrations in PBS was incubated with C6 cells for 24 hours, following 4 hour of 10 μL CCK-8 added for each well (5% CO$_2$, 37 °C). We prepared four wells for each sample. As for control groups, MTDR (M22426, Invitrogen; MA, USA) of different concentrations (PBS, DMSO < 1%) was applied as blank wells were set with no cells seeded, while negative controls were with no dye added. We then put plates into a microplate reader (Thermo Scientific 5250040, Thermo Fisher Scientific; MIT, USA). The optical density of each well measured at 450 nm

(OD_{450}) was recorded after 30 s plate shaking. To ensure the linear correlation between the cell number and OD_{450}, we also incubated cells with indicated numbers in complete DMEM for 2 hours and CCK-8 in basal culture media for four hours.

3.9. Localization of FO2 in C6 Cells

We first attached 14 mm tissue-culture treated glass coverslips (YA0350, Solarbio; Beijing, China) to each well bottom of 24-well plates. And homogeneous suspension with 5×10^4 cells per milliliter was seeded each well (one milliliter). After 24 hour incubation in complete DMEM media (5% CO_2, 37 °C), the cells were dyed with **FO2** (800 nM) and MTDR (100 nM) for 30 mins. Next, we used PBS to rinse the coverslips three times and fixed cells with 4% polyformaldehyde for 15 minutes at room temperature. And we applied another PBS rinse to these coverslips. Excessive PBS was removed by a stack of edge-touched water-absorbent tissue. Finally, the well-prepared cell coverslips were mounted on the slides with a small drop of anti-fade medium (ab104135, Abcom; Cambridge, UK).[63] Slides were stored at 4 °C before viewing.

The slides were observed under a confocal microscope (Olympus BX6, Olympus; Japan) with a 60× oil objective (1.35 NA). Excitation laser beams of 405 nm and 635 nm were switched on, and fluorescence signals were collected for **FO2** (λ_{Em} = 430/530 nm) and MTDR (λ_{Em} = 655/755 nm). In addition, the colocalization correlation between **FO2** and lysosomes was also tested. Images were recorded with a 2.0 plus zoom. Cellular colocalization analyses were performed following the instructions of Kenneth *et al.* by Pearson's correlation coefficient and Manders overlap coefficient using Image J (National Institutes of Health; MD, USA) and MATLAB (MathWorks; MA, USA).[64]

3.10. Cortical vascular imaging

All surgical instruments were autoclaved, and sterilized supplies like gloves, sterilized saline, and surgical towel were well prepared. Tribromoethanol (T903147, Macklin; Shanghai, China) was suitably stored at 4 °C in the dark. The 1.2% fresh working solution in normal saline was ready to use before operation. We used a depilatory cream to remove the head hair of mice and cleaned the surgical area with warm saline. A completely anesthetized mouse (tribromoethanol, i.p. 240 mg kg^{-1}) was fixed and disinfected with iodophors. Then we performed a craniotomy with a 1.5–2.0 mm window which was 1.5 mm posterior and 1.5 mm lateral to the bregma point. A three-milliliter coverslip was first immersed in warm saline and then used to cover the cranial window. A customized titanium plate was then glued to the skull with dental cement and formed an observation chamber (Fig. 3a and d). A warm blanket, covered with a sterilized towel, was applied during the surgery and observation. **FO2** (100 μL, one millimolar per liter in normal saline) was injected slowly into the retro-orbital venous sinus with an insulin injector (Fig. 3a).[65] And the anesthetized mice were fixed under the optical objective (×25, NA = 1.05, WD 2.0 mm, Olympus), and cortex vessels with **FO2** signals (495/540 nm) were recorded under the excitation laser at 810 nm (2.82 W, 2.0) μs per pixel.

3.11. *In vivo* mitochondrial imaging of cortical cells

Animals and craniotomy surgery were the same as *in vivo* cortex sensing after adding stereotactic injection. **FO2** (0.2 mM in disinfected normal saline) solution or **FO2** (0.2 mM) combined with 20 μM Mitotracker Red (M9940, Solarbio; Beijing, China) was filled in a 4 cm glass capillary with a tip of 0.1–0.2 mm diameter and injected with a stereotactic machine in the center area of the exposed window. The injection parameters were set with a speed of 80 nL min^{-1}. We injected **FO2** into different depths (200 μm, 400 μm, and 600 μm), in which each injection lasted for one minute and stopped for four minutes. During the stereotactic operation, wet cotton was used on the cranial window to prevent extensive fluid loss.[66]

The Olympus FVMPE-RS (Olympus; Japan) with a GaAsP enhanced photomultiplier tube, coupled with a Ti: sapphire mode-locked multi-photon laser (MaiTai eHPDS-OL), was used to collect images. A femtosecond laser beam was tuned to 810 nm (2.82 W, 2.0 μs per pixel) and passed through an infrared optimized water immersion objective (× 25, NA = 1.05, W.D. 2.0 mm, Olympus) and the water-filled optical chamber. The field of vision was optically zoomed (× 2.5), and signals (495/540 nm) were detected every 10 μm with a non-descanned detector (Fig. 3d).[67]

4. Summary

In summary, a biocompatible mitochondria targetable fluorescent probe, **FO2**, was designed, synthesized, and characterized. **FO2** exhibited excellent two-photon absorption properties, great biocompatibility, and high mitochondrial specificity. The marvelous two-photon absorption cross-section (1184 GM at 790 nm) was dozens to hundreds of times higher than those of almost all previously reported two-photon mitochondrial probes in aqueous solution.[11–13,36] The desired optical properties of **FO2** benefit *in vivo* bioimaging with a remarkable deep penetration of *ca.* 640 μm, superior to those of the other reported probes for mitochondrial imaging in this field, such as QBMP and Mito-TP-ClO.[11,43] Considering the fundamental functions of mitochondria among neurological diseases and rehabilitation,[68–70] **FO2** with the desired properties has a great potential for investigating the function and dysfunction of mitochondria in live animals through TPFI.

Author contributions

Z. C., L. L., Z. H., and T. Z. contributed equally to this work. L. L. and Z. H., investigation, data analysis, and writing original draft, review, and editing; X. W., S. H., and Z. C., conceptualization, supervision, validation, review, and editing; T. Z. and Y. Z. contributed significantly to the experimental design, data analysis and review; T. Z. also participated in the draft editing. X. C. participated in the cellular tests; Z. A., Z. W., F. C., K. S. and W. G. revised and offered constructive suggestions for the manuscript. All authors have approved the final version of the manuscript.

Data availability

The data to support the findings of this study are included in the paper, and further data are available from the corresponding author upon reasonable request.

Conflicts of interest

There are no conflicts to declare.

Acknowledgements

References

1 N. Pfanner, B. Warscheid and N. Wiedemann, Mitochondrial proteins: from biogenesis to functional networks, *Nat. Rev. Mol. Cell Biol.*, 2019, **20**(5), 267–284.

2 Q. Han, Y. Xie, J. D. Ordaz, A. J. Huh, N. Huang, W. Wu, N. Liu, K. A. Chamberlain, Z. H. Sheng and X. M. Xu, Restoring Cellular Energetics Promotes Axonal Regeneration and Functional Recovery after Spinal Cord Injury, *Cell Metab.*, 2020, **31**(3), 623–641.e8.

3 Y. Lai, P. Lin, M. Chen, Y. Zhang, J. Chen, M. Zheng, J. Liu, H. Du, R. Chen, X. Pan, N. Liu and H. Chen, Restoration of L-OPA1 alleviates acute ischemic stroke injury in rats via inhibiting neuronal apoptosis and preserving mitochondrial function, *Redox Biol.*, 2020, **34**, 101503.

4 V. Rangaraju, M. Lauterbach and E. M. Schuman, Spatially Stable Mitochondrial Compartments Fuel Local Translation during Plasticity, *Cell*, 2019, **176**(1-2), 73–84.e15.

5 R. Cartoni, M. W. Norsworthy, F. Bei, C. Wang, S. Li, Y. Zhang, C. V. Gabel, T. L. Schwarz and Z. He, The Mammalian-Specific Protein Armcx1 Regulates Mitochondrial Transport during Axon Regeneration, *Neuron*, 2016, **92**(6), 1294–1307.

6 P. Sahu and N. Mazumder, Advances in adaptive optics-based two-photon fluorescence microscopy for brain imaging, *Lasers Med. Sci.*, 2020, **35**(2), 317–328.

7 F. Helmchen and W. Denk, Deep tissue two-photon microscopy, *Nat. Methods*, 2005, **2**(12), 932–940.

8 J. Lecoq, N. Orlova and B. F. Grewe, Wide. Fast. Deep: Recent Advances in Multiphoton Microscopy of In Vivo Neuronal Activity, *J. Neurosci.*, 2019, **39**(46), 9042–9052.

9 S. Jakobs, T. Stephan, P. Ilgen and C. Brüser, Light Microscopy of Mitochondria at the Nanoscale, *Annu. Rev. Biophys.*, 2020, **49**, 289–308.

10 H. Zhu, J. Fan, J. Du and X. Peng, Fluorescent Probes for Sensing and Imaging within Specific Cellular Organelles, *Acc. Chem. Res.*, 2016, **49**(10), 2115–2126.

11 Y. P. Yang, F. J. Qi, Y. P. Qian, X. Z. Bao, H. C. Zhang, B. Ma, F. Dai, S. X. Zhang and B. Zhou, Developing Push-Pull Hydroxylphenylpolyenylpyridinium Chromophores as Ratiometric Two-Photon Fluorescent Probes for Cellular and Intravital Imaging of Mitochondrial NQO1, *Anal. Chem.*, 2021, **93**(4), 2385–2393.

12 J. X. Zhang, M. Pan and C. Y. Su, Synthesis, photophysical properties and in vitro evaluation of a chlorambucil conjugated ruthenium(II) complex for combined chemo-photodynamic therapy against HeLa cells, *J. Mater. Chem. B*, 2017, **5**(24), 4623–4632.

13 G. Niu, R. Zhang, Y. Gu, J. Wang, C. Ma, R. T. K. Kwok, J. W. Y. Lam, H. H. Sung, I. D. Williams, K. S. Wong, X. Yu and B. Z. Tang, Highly photostable two-photon NIR AIEgens with tunable organelle specificity and deep tissue penetration, *Biomaterials*, 2019, **208**, 72–82.

14 Y. Niko, H. Moritomo, H. Sugihara, Y. Suzuki, J. Kawamata and G. I. Konishi, A novel pyrene-based two-photon active fluorescent dye efficiently excited and emitting in the 'tissue optical window (650-1100 nm)', *J. Mater. Chem. B*, 2015, **3**(2), 184–190.

15 P. Ning, J. Jiang, L. Li, S. Wang, H. Yu, Y. Feng, M. Zhu, B. Zhang, H. Yin, Q. Guo and X. Meng, A mitochondria-targeted ratiometric two-photon fluorescent probe for biological zinc ions detection, *Biosens. Bioelectron.*, 2016, **77**, 921–927.

16 J. Fu, L. A. Padilha, D. J. Hagan, E. W. Van Stryland, O. V. Przhonska, M. V. Bondar, Y. L. Slominsky and A. D. Kachkovski, Molecular structure—two-photon absorption property relations in polymethine dyes, *J. Opt. Soc. Am. B*, 2007, **24**(1), 56–66.

17 K. Yuzhan; Q. Peng; S. K. Maji; Y. Tong; H. Yu; Y. Zhao; P. Ramamurthyc and A. Ajayaghosh, A ratiometric fluorescent molecular probe with enhanced two-photon response upon Zn 2 binding for *in vitro* and *in vivo* bioimaging.

18 D. S. Philips, S. Sreejith, T. He, N. V. Menon, P. Anees, J. Mathew, S. Sajikumar, Y. Kang, M. C. Stuparu, H. Sun, Y. Zhao and A. Ajayaghosh, A Three-Photon Active Organic Fluorophore for Deep Tissue Ratiometric Imaging of Intracellular Divalent Zinc, *Chem. – Asian J.*, 2016, **11**(10), 1523–1527.

19 W. Yang, P. S. Chan, M. S. Chan, K. F. Li, P. K. Lo, N. K. Mak, K. W. Cheah and M. S. Wong, Two-photon fluorescence probes for imaging of mitochondria and lysosomes, *Chem. Commun.*, 2013, **49**(33), 3428–3430.

20 K. D. Belfield, M. V. Bondar, A. R. Morales, L. A. Padilha, O. V. Przhonska and X. Wang, Two-photon STED spectral

determination for a new V-shaped organic fluorescent probe with efficient two-photon absorption, *ChemPhysChem*, 2011, **12**(15), 2755–2762.

21 Q. Pei and Y. Yang, Efficient Photoluminescence and Electroluminescence from a Soluble Polyfluorene, *J. Am. Chem. Soc.*, 1996, **118**(31), 7416–7417.

22 A. M. Mahmoud, P. de Jongh, S. Briere, M. Chen, C. J. Nowell, A. P. R. Johnston, T. P. Davis, D. M. Haddleton and K. Kempe, Carboxylated Cy5-Labeled Comb Polymers Passively Diffuse the Cell Membrane and Target Mitochondria, *ACS Appl. Mater. Interfaces*, 2019, **11**(34), 31302–31310.

23 D. Lombardo, M. A. Kiselev, S. Magazù and P. Calandra, Amphiphiles Self-Assembly: Basic Concepts and Future Perspectives of Supramolecular Approaches, *Adv. Condens. Matter Phys.*, 2015, **2015**, 151683.

24 C. Laperchia, A. L. Allegra Mascaro, L. Sacconi, A. Andrioli, A. Matte, L. De Franceschi, G. Grassi-Zucconi, M. Bentivoglio, M. Buffelli and F. S. Pavone, Two-photon microscopy imaging of thy1GFP-M transgenic mice: a novel animal model to investigate brain dendritic cell subsets *in vivo*, *PLoS One*, 2013, **8**(2), e56144.

25 P. O'Herron, P. M. Summers, A. Y. Shih, P. Kara and J. J. Woodward, In vivo two-photon imaging of neuronal and brain vascular responses in mice chronically exposed to ethanol, *Alcohol*, 2020, **85**, 41–47.

26 T. Geiller, B. Vancura, S. Terada, E. Troullinou, S. Chavlis, G. Tsagkatakis, P. Tsakalides, K. Ocsai, P. Poirazi, B. J. Rozsa and A. Losonczy, Large-Scale 3D Two-Photon Imaging of Molecularly Identified CA1 Interneuron Dynamics in Behaving Mice, *Neuron*, 2020, **108**(5), 968–983.e9.

27 O. Garaschuk, R. I. Milos and A. Konnerth, Targeted bulk-loading of fluorescent indicators for two-photon brain imaging in vivo, *Nat. Protoc.*, 2006, **1**(1), 380–386.

28 M. K. Hazra and B. Bagchi, Non-equilibrium solvation dynamics in water-DMSO binary mixture: Composition dependence of non-linear relaxation, *J. Chem. Phys.*, 2018, **149**(8), 084501.

29 B. Bagchi, The amphiphilic effect: The diverse but intimate world of aqueous binary mixtures, in *Water in Biological and Chemical Processes: From Structure and Dynamics to Function (Cambridge Molecular Science)*, Cambridge University Press, Cambridge, 2013, pp. 243–260.

30 A. Jiang, G. Chen, J. Xu, Y. Liu, G. Zhao, Z. Liu, T. Chen, Y. Li and T. D. James, Ratiometric two-photon fluorescent probe for in situ imaging of carboxylesterase (CE)-mediated mitochondrial acidification during medication, *Chem. Commun.*, 2019, **55**(76), 11358–11361.

31 H. Cho, Y. Y. Cho, M. S. Shim, J. Y. Lee, H. S. Lee and H. C. Kang, Mitochondria-targeted drug delivery in cancers, *Biochim. Biophys. Acta, Mol. Basis Dis.*, 2020, **1866**(8), 165808.

32 R. Guo, J. Yin, Y. Ma, Q. Wang and W. Lin, A novel mitochondria-targeted rhodamine analogue for the detection of viscosity changes in living cells, zebra fish and living mice, *J. Mater. Chem. B*, 2018, **6**(18), 2894–2900.

33 M. Peng, J. Yin and W. Lin, Tracking mitochondrial viscosity in living systems based on a two-photon and near red probe, *New J. Chem.*, 2019, **43**(43), 16945–16949.

34 J. Mei, N. L. Leung, R. T. Kwok, J. W. Lam and B. Z. Tang, Aggregation-Induced Emission: Together We Shine, United We Soar!, *Chem. Rev.*, 2015, **115**(21), 11718–11940.

35 Q. Chen, H. Fang, X. Shao, Z. Tian, S. Geng, Y. Zhang, H. Fan, P. Xiang, J. Zhang, X. Tian, K. Zhang, W. He, Z. Guo and J. Diao, A dual-labeling probe to track functional mitochondria–lysosome interactions in live cells, *Nat. Commun.*, 2020, **11**(1), 6290.

36 Z. Zheng, T. Zhang, H. Liu, Y. Chen, R. T. K. Kwok, C. Ma, P. Zhang, H. H. Y. Sung, I. D. Williams, J. W. Y. Lam, K. S. Wong and B. Z. Tang, Bright Near-Infrared Aggregation-Induced Emission Luminogens with Strong Two-Photon Absorption, Excellent Organelle Specificity, and Efficient Photodynamic Therapy Potential, *ACS Nano*, 2018, **12**(8), 8145–8159.

37 X. Wang, D. M. Nguyen, C. O. Yanez, L. Rodriguez, H. Y. Ahn, M. V. Bondar and K. D. Belfield, High-fidelity hydrophilic probe for two-photon fluorescence lysosomal imaging, *J. Am. Chem. Soc.*, 2010, **132**(35), 12237–12239.

38 F. Miao, W. Zhang, Y. Sun, R. Zhang, Y. Liu, F. Guo, G. Song, M. Tian and X. Yu, Novel fluorescent probes for highly selective two-photon imaging of mitochondria in living cells, *Biosens. Bioelectron.*, 2014, **55**, 423–429.

39 J. Shen, T. W. Rees, Z. Zhou, S. Yang, L. Ji and H. Chao, A mitochondria-targeting magnetothermogenic nanozyme for magnet-induced synergistic cancer therapy, *Biomaterials*, 2020, **251**, 120079.

40 M. Takezaki, R. Kawakami, S. Onishi, Y. Suzuki, J. Kawamata, T. Imamura, S. Hadano, S. Watanabe and Y. Niko, Integrated Fluorescent Nanoprobe Design for High-Speed In Vivo Two-Photon Microscopic Imaging of Deep-Brain Vasculature in Mice, *Adv. Funct. Mater.*, 2021, **31**(20), 2010698.

41 W. Zhuang, L. Yang, B. Ma, Q. Kong, G. Li, Y. Wang and B. Z. Tang, Multifunctional Two-Photon AIE Luminogens for Highly Mitochondria-Specific Bioimaging and Efficient Photodynamic Therapy, *ACS Appl. Mater. Interfaces*, 2019, **11**(23), 20715–20724.

42 H. He, W. Zhuang, B. Ma, X. Su, T. Yu, J. Hu, L. Chen, R. Peng, G. Li and Y. Wang, Oxidation-Responsive and Aggregation-Induced Emission Polymeric Micelles with Two-Photon Excitation for Cancer Therapy and Bioimaging, *ACS Biomater. Sci. Eng.*, 2019, **5**(5), 2577–2586.

43 G. J. Mao, G. Q. Gao, Z. Z. Liang, Y. Y. Wang, L. Su, Z. X. Wang, H. Zhang, Q. J. Ma and G. Zhang, A mitochondria-targetable two-photon fluorescent probe with a far-red to near-infrared emission for sensing hypochlorite in biosystems, *Anal. Chim. Acta*, 2019, **1081**, 184–192.

44 F. Schueder, J. Lara-Gutiérrez, B. J. Beliveau, S. K. Saka, H. M. Sasaki, J. B. Woehrstein, M. T. Strauss, H. Grabmayr, P. Yin and R. Jungmann, Multiplexed 3D super-resolution imaging of whole cells using spinning disk confocal microscopy and DNA-PAINT, *Nat. Commun.*, 2017, **8**(1), 2090.

45 D. Neumann, J. Bückers, L. Kastrup, S. W. Hell and S. Jakobs, Two-color STED microscopy reveals different degrees of colocalization between hexokinase-I and the three human VDAC isoforms, *PMC Biophys.*, 2010, **3**(1), 4.

46 R. Rupprecht, V. Papadopoulos, G. Rammes, T. C. Baghai, J. Fan, N. Akula, G. Groyer, D. Adams and M. Schumacher, Translocator protein (18 kDa) (TSPO) as a therapeutic target for neurological and psychiatric disorders, *Nat. Rev. Drug Discovery*, 2010, **9**(12), 971–988.

47 W. Neupert and J. M. Herrmann, Translocation of proteins into mitochondria, *Annu. Rev. Biochem.*, 2007, **76**, 723–749.

48 S. Stoldt, T. Stephan, D. C. Jans, C. Brüser, F. Lange, J. Keller-Findeisen, D. Riedel, S. W. Hell and S. Jakobs, Mic60 exhibits a coordinated clustered distribution along and across yeast and mammalian mitochondria, *Proc. Natl. Acad. Sci. U. S. A.*, 2019, **116**(20), 9853–9858.

49 E. Fanizza, R. M. Iacobazzi, V. Laquintana, G. Valente, G. Caliandro, M. Striccoli, A. Agostiano, A. Cutrignelli, A. Lopedota, M. L. Curri, M. Franco, N. Depalo and N. Denora, Highly selective luminescent nanostructures for mitochondrial imaging and targeting, *Nanoscale*, 2016, **8**(6), 3350–3361.

50 D. M. Shcherbakova, O. M. Subach and V. V. Verkhusha, Red fluorescent proteins: advanced imaging applications and future design, *Angew. Chem., Int. Ed.*, 2012, **51**(43), 10724–10738.

51 T. Rappitsch and S. M. Borisov, Carbazole- and Fluorene-Fused Aza-BODIPYs: NIR Fluorophores with High Brightness and Photostability, *Chem. – Eur. J.*, 2021, **27**(41), 10685–10692.

52 G. V. Bünau, *Birks, J. J. B. B. P. C., Photophysics of Aromatic Molecules*, Wiley-Interscience, London, 704 Seiten. Preis: 210s, 1970, vol. 74, pp. 1294–1295.

53 M. Collot, S. Bou, T. K. Fam, L. Richert, Y. Mély, L. Danglot and A. S. Klymchenko, Probing Polarity and Heterogeneity of Lipid Droplets in Live Cells Using a Push-Pull Fluorophore, *Anal. Chem.*, 2019, **91**(3), 1928–1935.

54 C. Reichardt, Solvatochromic Dyes as Solvent Polarity Indicators, *J. Chem. Rev.*, 1994, **94**, 2319–2358.

55 E. Bosch and M. Rosés, Relationship between ET polarity and composition in binary solvent mixtures, *J. Chem. Soc., Faraday Trans.*, 1992, **88**(24), 3541–3546.

56 Y. Guo, K. Jiang, Z. Shen, G. Zheng, L. Fan, R. Zhao and J. Shao, A Small Molecule Nanodrug by Self-Assembly of Dual Anticancer Drugs and Photosensitizer for Synergistic near-Infrared Cancer Theranostics, *ACS Appl. Mater. Interfaces*, 2017, **9**(50), 43508–43519.

57 W. Niu, L. Guo, Y. Li, S. Shuang, C. Dong and M. S. Wong, Highly Selective Two-Photon Fluorescent Probe for Ratiometric Sensing and Imaging Cysteine in Mitochondria, *Anal. Chem.*, 2016, **88**(3), 1908–1914.

58 L. Song, E. Hennink, I. T. Young and H. J. Tanke, Photobleaching kinetics of fluorescein in quantitative fluorescence microscopy, *Biophys. J.*, 1995, **68**(6), 2588–2600.

59 M. Levitus, Tutorial: measurement of fluorescence spectra and determination of relative fluorescence quantum yields of transparent samples, *Methods Appl. Fluoresc.*, 2020, **8**(3), 033001.

60 S. de Reguardati, J. Pahapill, A. Mikhailov, Y. Stepanenko and A. Rebane, High-accuracy reference standards for two-photon absorption in the 680–1050 nm wavelength range, *Opt. Express*, 2016, **24**(8), 9053–9066.

61 C. Xu and W. W. Webb, Measurement of two-photon excitation cross sections of molecular fluorophores with data from 690 to 1050 nm, *J. Opt. Soc. Am. B*, 1996, **13**(3), 481–491.

62 M. A. Albota, C. Xu and W. W. Webb, Two-Photon Fluorescence Excitation Cross Sections of Biomolecular Probes from 690 to 960 nm, *Appl. Opt.*, 1998, **37**(31), 7352–7356.

63 Y. Pang, K. Simpson, J. J. Miguel-Hidalgo and R. Savich, Neuron/Oligodendrocyte Myelination Coculture, *Methods Mol. Biol.*, 2018, **1791**, 131–144.

64 K. W. Dunn, M. M. Kamocka and J. H. McDonald, A practical guide to evaluating colocalization in biological microscopy, *Am. J. Physiol.*, 2011, **300**(4), C723–C742.

65 C. D. Steel, A. L. Stephens, S. M. Hahto, S. J. Singletary and R. P. Ciavarra, Comparison of the lateral tail vein and the retro-orbital venous sinus as routes of intravenous drug delivery in a transgenic mouse model, *Lab. Anim.*, 2008, **37**(1), 26–32.

66 H. Liu, J. Wang, Z. Zhuang, J. He, W. Wen, P. Qiu and K. Wang, Visualizing astrocytes in the deep mouse brain *in vivo*, *J. Biophotonics*, 2019, **12**(7), e201800420.

67 J. Sword, T. Masuda, D. Croom and S. A. Kirov, Evolution of neuronal and astroglial disruption in the peri-contusional cortex of mice revealed by in vivo two-photon imaging, *Brain*, 2013, **136**(Pt 5), 1446–1461.

68 M. Calvo-Rodriguez and B. J. Bacskai, Mitochondria and Calcium in Alzheimer's Disease: From Cell Signaling to Neuronal Cell Death, *Trends Neurosci.*, 2021, **44**(2), 136–151.

69 M. J. Devine and J. T. Kittler, Mitochondria at the neuronal presynapse in health and disease, *Nat. Rev. Neurosci.*, 2018, **19**(2), 63–80.

70 R. Cartoni, G. Pekkurnaz, C. Wang, T. L. Schwarz and Z. He, A high mitochondrial transport rate characterizes CNS neurons with high axonal regeneration capacity, *PLoS One*, 2017, **12**(9), e0184672.